Quasi-Static Assembly of Compliantly Supported Rigid Parts

Daniel E. Whitney

Abstract. Geometric and force equilibrium conditions for successfully mating rigid parts are presented. The action of the Remote Center Compliance (RCC) is explained. Guidelines for choosing RCC parameters are presented. Models of insertion force behavior are verified by experimental data.

I. Introduction

The goal of this paper is to describe rigid part mating, that is, the assembly of parts that do not substantially deform during assembly. Assembly is a geometric problem and, if parts were identical, perfectly made, and perfectly positioned, assembly would always be successful and free of excessive mating force. Practical constraints such as cost and technical limitations cause parts to differ, machines and jigs to wear and, consequently, parts to be misplaced or misaligned at the moment of assembly. The theory and experiments described below delineate the events that occur and forces that arise during error-corrupted assembly. From this we can obtain techniques for increasing the likelihood of successful assembly without recourse to expensive methods like eliminating the errors in advance or sensing and correcting them on the fly.

This paper brings together new work plus several years' prior work by the author and his colleagues which has not previously been integrated and presented in one place; hence its length. A large part consists of reformulations of work by Simunovic [1975, 1979]. Other portions appeared in [Nevins et al. 1974a, 1974b, 1975, 1976, 1977, Drake 1977]. [Watson, 1976, McCallion and Wong 1975. Savischenko and Bespalov 1965, Andreev and Laktionev 1966, 1969, Laktionev and Andreev 1966, Karelin and Girel, 1967, Gusev 1969, Andreev 1972, Arai and Kinoshita 1981, Ohwovoriole 1980] also treat aspects of the problem. [Arai and Kinoshita 1981] analyze the assembly of a rigidly supported rigid peg into a hole in a compliantly supported worktable. [Ohwovoriole 1980]

contains a complete kinematic and force analysis of rigid peg-hole assembly in the one-and two-point contact phases only, utilizing an arbitrary insertion force vector. No assumptions about the source of this vector are made, and no mating force histories are discussed. *Wedging* is studied, but using a different definition from that used here and yielding different conclusions. In [Arai and Kinoshita 1981], the assembly force is supplied by the interaction of the parts and the compliances and, because no small angle approximations are made, closed form solutions to the two-point contact case cannot be obtained.

It will be shown (in agreement with [Arai and Kinoshita 1981]) that part geometry, the stiffness of jigs or grippers supporting the parts, and friction between the parts are the major factors in rigid part mating. Equations for mating force versus insertion distance will be derived, along with limitations on allowed error and recommendations for compliant gripper or jig design which help avoid unsuccessful assembly. All equations are worked out for the case of round pegs and round chamfered holes (modeled as flat tabs and slots) with constant and identical coefficient of friction acting at all contact points. Small angle approximations are used so that explicit solutions can be obtained and several interesting properties derived and studied. Gravity and inertia are ignored. Experimental verifications utilize three-dimensional parts.

During assembly, parts must be supported by jigs, fixtures, hands, grippers, etc. These supports have some compliance, either by design or accident. Rigid part mating theory can then be said to apply to parts which are rigid compared to the supports. Modeling the supports is an important aspect of part mating theory. In this paper, a unified and fairly general method of modeling supports will be used, and the equations for mating forces will contain the main characteristics of the modeled supports in parametric form so that the influence of different values of support parameters can be studied.

The importance and desirable features of a properly designed support are major results of part mating theory. Supports with especially good characteristics are called remote center compliances (RCC's) [Drake 1977, Watson 1976]. Although RCC's themselves will not be discussed in this paper, the reasons why they aid part mating will be explained using the parameterized equations.

The paper is organized as follows: Section 2 contains general descriptions and definitions. Section 3 analyzes the geometric conditions of round peg-hole assembly, while Section 4 derives the contact forces between parts and concludes with sufficient conditions to avoid *wedging* and *jamming*. Section 5 derives the insertion force equations and, using a simplified support model, shows how the RCC helps avoid jamming and reduces mating force. Section 6 presents complete mating force equations and experimental verifications. Section 7 is an analysis of wedging. Section 8 concludes the paper and summarizes the results.
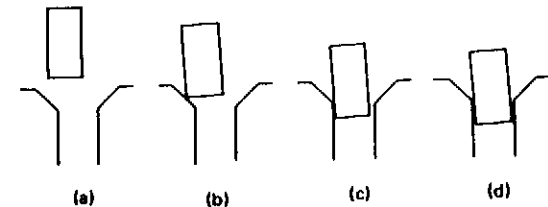
Figure 1
Four stages of assembly: approach, chamfer crossing, one-point contact, two-point contact.

2. Definitions

Consideration of typical part mating geometry shows that a mating event has these stages (see Figure 1):

- approach,
- chamfer crossing,
- one-point contact,
- two-point contact.

(Under some circumstances, one-point contact or line-contact can recur after a period of two-point contact.)

In general, the part rotates and translates during mating as initial lateral and angular errors between the parts are corrected. Compliant supports must therefore provide both lateral and angular compliance for at least one of the mating parts. If certain symmetry conditions are satisfied, then any compliant support can be represented mathematically by a *compliance center* plus the support's stiffness *laterally at*, and *angularly around*, this center (Figure 2). That is, the compliance matrix of the support is diagonal in coordinates whose origin is at the compliance center. The support is assumed to attach to the part at this point, marked $\otimes$ in Figure 2. The forces and moments applied by the support are re-expressed in peg tip coordinates in terms of F_x, F_z, and M. This method of representing supports was introduced by Simunovic [1979] and is a powerful tool for analyzing part mating because so many supports can be represented this way.

A part mating event can then be represented by the path of the supported part (constrained by its shape and the shape of the other mating part), the path of the support (constrained by the robot or machine doing the assembly), the forces and moments applied to the part by the compliances of the support as these paths deviate, and the forces applied by the contact and friction forces
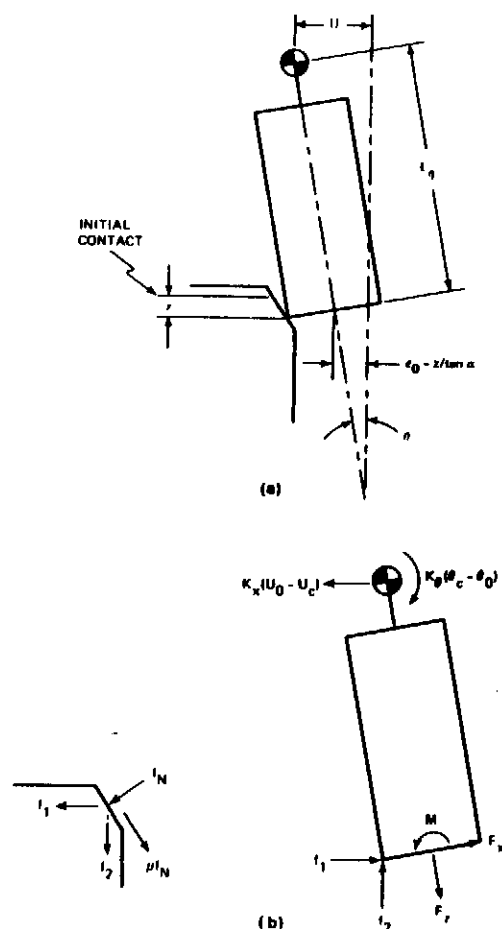
Figure 2
Rigid peg supported compliantly by lateral spring K_x and angular spring K_θ at a distance L_g from peg's tip.

between the two parts.

Simunovic showed that successful part mating depends on maintaining certain relationships between the applied forces and moments during two-point contact. This guarantees avoidance of *jamming*, in which the forces applied to the part point in the wrong direction. A similar phenomenon, called *wedging*, can occur if two-point contact occurs too early in the mating. Avoidance of wedging depends on control of initial condition errors between the parts.

These topics will now be discussed in more detail.

3. Geometry of Part Mating

We begin by developing the equations which describe the path of the compliance center ⊗ while the part traverses the phases of chamfer crossing, one-point contact, and two-point contact. The compliance center's location is a basic support design parameter. It will be placed at an arbitrary point on the peg's axis for generality, and the optimum location will be derived later. We assume throughout that the angle θ between peg and hole axes is small and that the assembly device carries the support on a path parallel to the hole's axis while the compliance center ⊗ moves with the peg. (A more complete analysis would allow a general angle between the path of the support and the hole's axis.) Until the peg touches the chamfer or hole the compliances are relaxed.

Figure 3
Definition of terms for geometric analysis of part mating. The arrow indicates direction of motion of the support.

In this state, the initial lateral and angular errors ϵ_0 and θ_0 (Figure 3) combine to place the compliance center a distance U_0 to one side of the hole's axis. Once contact occurs the compliance will deform. These deformations will be accounted for by deviations $U_0 - U$ and $\theta - \theta_0$ from the rest position.

3.1 Chamfer Crossing. The geometry of peg and hole during chamfer crossing is shown in Figure 4a and the forces are shown in Figure 4b. The chamfer is described by its angle α and width w. The geometry is described by

$$U_0 = \epsilon_0 + L_g \theta_0 \tag{1}$$

$$U = L_g \theta - \frac{z}{\tan \alpha} + \epsilon_0 \tag{2}$$

where z ranges from zero at the initial contact to $\epsilon_0' \tan \alpha$ when the tip of the peg reaches the bottom of the chamfer and one-point contact begins. We define

$$\epsilon_0' = \epsilon_0 - cR \tag{3}$$

where

$$c = \frac{R - r}{R} \tag{4}$$

INITIAL
CONTACT

$\epsilon_0 - z/\tan\alpha$

(a)

$K_x(U_0 - U_c)$ $K_\theta(\theta_c - \theta_0)$

l_N

l_1

l_2 μl_N

M

F_x

l_1

l_2 F_r

(b)

Figure 4
Geometry (a) and forces (b) during chamfer crossing.

R and r are hole and peg radius respectively, and c is called the *clearance ratio*.

A force balance yields

$$f_1 = f_N B$$
$$f_2 = f_N A$$
$$\tag{5}$$

where

$$A = \cos\alpha + \mu\sin\alpha$$

$$B = \sin\alpha - \mu\cos\alpha$$

and μ is the coefficient of friction. The contact and applied spring support forces can be expressed in coordinates attached to the peg's tip by the *contact forces*

$$F_z = -f_1$$
$$F_x = f_2 \tag{6a}$$
$$M = f_2 r$$

and the *support forces*

$$F_z = -K_z(U_0 - U)$$
$$M = K_z L_\theta(U_0 - U) - K_\theta(\theta - \theta_0) \tag{6b}$$

Combining (1) through (6) yields expressions for θ and U during chamfer crossing

$$\theta = \theta_0 + \frac{K_z(z/\tan\alpha)(L_\theta B - rA)}{(K_z L_\theta^2 + K_\theta)B - K_z L_\theta rA} \tag{7}$$

and

$$U = U_0 - \frac{K_\theta(z/\tan\alpha)B}{(K_z L_\theta^2 + K_\theta)B - K_z L_\theta rA} \tag{8}$$

3.2 One-Point Contact. The forces acting during one-point contact are shown in Figure 5. A derivation analogous to the above, beginning with the geometric constraint

$$U = cR + L_\theta\theta - \ell\theta \tag{9}$$

yields the following expressions for θ and U during one-point contact.

$$\theta = \frac{C(\epsilon_0' + L_\theta\theta_0) + K_\theta\theta_0}{C(L_\theta - \ell) + K_\theta} \tag{10}$$

where

$$C = K_z(L_\theta - \ell - \mu r)$$

and

$$U = U_0 - \frac{K_\theta(\epsilon_0' + \ell\theta_0)}{C(L_\theta - \ell) + K_\theta} \tag{11}$$
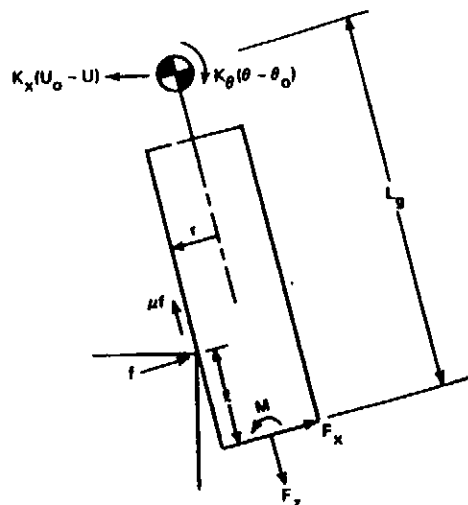
Figure 5
Forces acting during one-point contact.

Insertion depth ℓ is defined to be zero just as the tip of the peg reaches the bottom of the chamfer. Setting $\ell = 0$ in (10) yields θ_1, the value of θ just as one-point contact begins

$$\theta_1 = \theta_0 + \frac{K_x(L_g - \mu r)\epsilon_0^l}{K_x L_g(L_g - \mu r) + K_\theta} \tag{12}$$

3.3 Two-Point Contact. Two-point contact will be analyzed for only one of the four possibilities of initial error ($\pm\epsilon_0, \pm\theta_0$). The derivations for the other cases are similar.

Geometric compatibility between peg and hole during two-point contact is governed by

$$R = \frac{\ell}{2} \tan\theta + r \cos\theta \tag{13}$$

which, for small θ, becomes

$$\ell\theta = 2cR = cD, \quad \text{constant} \tag{14}$$

It is easy to show that θ must be less than θ_m, defined by

$$\theta_m = \sqrt{2c} \tag{15}$$
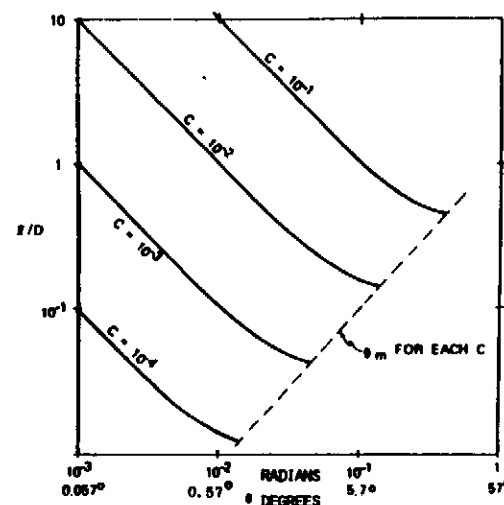
Figure 6
Wobble angle versus insertion depth.

during two-point contact. A smaller upper limit on θ in two-point contact, based on friction considerations, is discussed in the next section. Equations (13) and (15) are plotted in Figure 6.

To determine when two-point contact begins, we note first that during one-point contact, the geometric constraint is

$$U_0 - U = \epsilon_0^l + L_g(\theta_0 - \theta) + \ell\theta \tag{16}$$

Substituting (14) into (16) and calling θ equal to θ_2 where two-point contact begins, we have

$$U_0 - U_2 = \epsilon_0'' + L_g(\theta_0 - \theta_2) \tag{17}$$

where

$$\epsilon_0'' = \epsilon_0 + cR \tag{18}$$

Equation (17) relates $\theta = \theta_2$ and $U = U_2$ just as two-point contact starts. Using (17) in a force balance analysis similar to the above (see Figure 7) yields for U and θ at onset of two-point contact:

$$\theta_2 = \theta_0 + \frac{K_x\epsilon_0''(L_g - \ell_2 - \mu r)}{K_x L_g^2 + K_\theta - K_x L_g(\ell_2 + \mu r)} \tag{19}$$
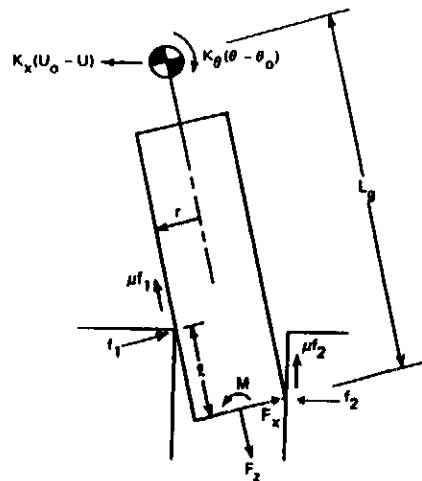
Figure 7
Forces acting during two-point contact.

and

$$U_2 = U_0 - \frac{K_\theta \epsilon_0''}{K_z L_g^2 + K_\theta - K_z L_g(\ell_2 + \mu r)} \qquad (20)$$

To find ℓ_2, the insertion depth at which two-point contact begins, substitute (14) into (19). This yields a quadratic for ℓ_2

$$\alpha \ell_2^2 - \beta \ell_2 + \gamma = 0 \qquad (21)$$

where

$$\alpha = K_z(\epsilon_0'' + L_g \theta_0)$$
$$\beta = (L_g - \mu r)\alpha + K_z L_g cD + K_\theta \theta_0 \qquad (22)$$
$$\gamma = cD(K_z L_g^2 + K_\theta - K_z L_g \mu r)$$

so that

$$\ell_2 = \frac{\beta - \sqrt{\beta^2 - 4\alpha\gamma}}{2\alpha} \qquad (23)$$

and

$$\ell_2' = \frac{\beta + \sqrt{\beta^2 - 4\alpha\gamma}}{2\alpha} \qquad (24)$$
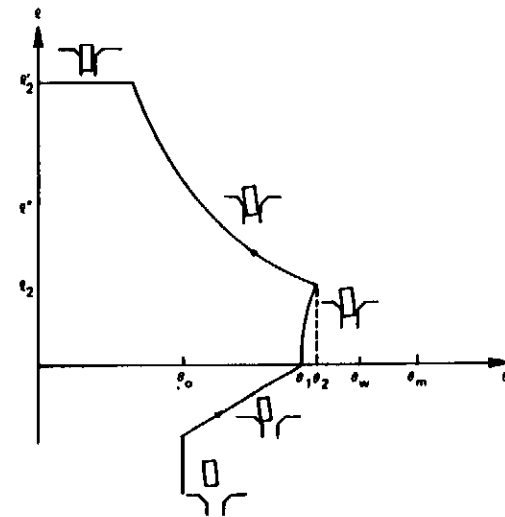
Figure 8
Schematic life cycle plot of insertion.

The existence of two solutions shows that there is not only a value ℓ_2 at which two-point contact begins but also a value $\ell_2' > \ell_2$ at which two-point contact ends and one-point contact resumes. Once ℓ_2 is known, we can use equation (13) or (14) to find θ_2.

If we assume $K_\theta \gg K_z L_g^2$ and $K_\theta \theta_0 \gg \mu K_z \epsilon_0'' r$ we obtain the approximations

$$\ell_2 \simeq \frac{cD}{\theta_0} \qquad (25)$$

and

$$\ell_2' \simeq \frac{K_\theta \theta_0}{K_z \epsilon_0''} - \ell_2 \qquad (26)$$

These assumptions are, coincidentally, satisfied by all current designs of Remote Center Compliances and a wide range of values of θ_0, ϵ_0, μ, r, and L_g (see section 5). Also, if L_g and θ_0 are small enough, there will be no solution to (21) implying that two-point contact cannot occur.

3.4 Discussion. Figure 8 summarizes the above results as a crossplot of ℓ vs. θ. Figure 8 is called a life cycle plot of a peg-in-hole insertion. The terms ℓ'' and θ_w will be defined in later sections, where experimental verification will be presented.
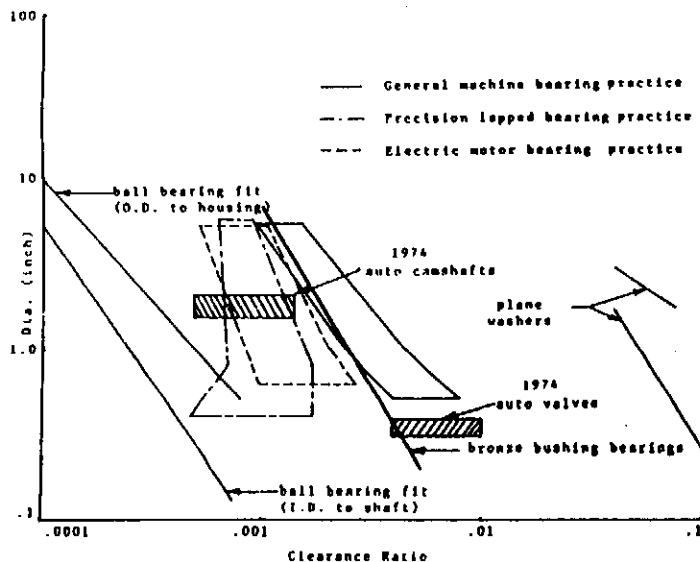
Figure 9
Survey of dimensioning practice for rigid parts.

Dimensioning practice was surveyed in typical machined parts [Kondoleon 1976] with the result that clearance ratio c is well (though not perfectly) correlated with part type and use. Figure 9 shows the survey results. The combination of Figures 6 and 9 indicates how difficult an insertion of a given type part might be, based on the geometric parameters. A complete discussion of this point is deferred to the next section. Note that the assumption of small angles is borne out for the part types surveyed.

Finally, note that most part mating difficulties occur during two-point contact. Measures taken to increase the value of ℓ_2 or to prevent two-point contact will result in more reliable part mating. The most effective of these measures is making L_g as small as possible. This is a major function of the RCC.

4. Forces Acting During Assembly: Wedging and Jamming

In order to determine whether assembly will succeed or fail, it is necessary to consider the forces acting on the parts in addition to the geometric compatibilities treated above. Two phenomena were defined by Simunovic, *wedging* and *jamming*, to describe situations in which the peg seems to stick in the hole

during two-point contact. Jamming will be considered first.

Jamming is a condition in which the peg will not move because the forces and moments applied to the peg through the support are in the wrong proportions. The correct proportions were orginally presented by Simunovic [1975]. A simpler derivation and more complete exploration of the problem are presented here.

We follow Simunovic's approach and express the applied insertion force in terms of F_z, F_x, and M at or about the peg's tip, as shown in Figure 10. We wish to find equilibrium-sliding-in conditions between the applied forces and the reactions f_1 and f_2.

Simunovic's results are based on ignoring the angle of tilt of the peg with respect to the hole. The equilibrium equations which describe the peg sliding in are then given by

$$F_z = \mu(f_1 + f_2) \qquad (25)$$
$$F_x = f_2 - f_1 \qquad (26)$$
$$M = f_1\ell - \mu r(f_2 - f_1) \qquad (27)$$

Combining these equations yields

$$\frac{M}{rF_z} = \frac{\ell}{2r\mu} - \frac{F_x}{F_z}\left(\frac{\ell}{2r} + \mu\right) \qquad (28)$$

Define

$$\lambda = \frac{\ell}{2r\mu} \qquad (29)$$

Then equation (28) can be expressed as

$$y = mx + b \qquad (30)$$

where

$$y = \frac{M}{rF_z} \qquad (31)$$
$$x = \frac{F_x}{F_z} \qquad (32)$$
$$m = -\mu(1 + \lambda) \qquad (33)$$
$$b = \lambda \qquad (34)$$

If one draws the peg leaning the other way, one obtains the same equation, except

$$b = -\lambda \qquad (35)$$

To finish the derivation, we must first consider the four possible one-point contacts, of which two will suffice for illustration (see Figure 10).
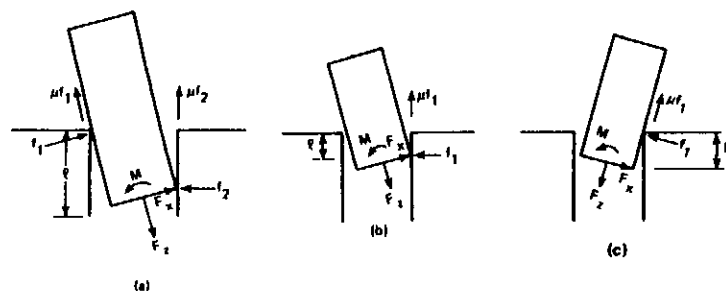
Figure 10
Applied forces and reaction forces. (a) Peg in two-point contact. (b)-(c) One point contacts.

For Figure 10b, the equilibrium equations are

$$M + \mu r F_x = 0 \tag{36}$$

$$F_z - \mu F_x = 0 \tag{37}$$

or

$$\frac{F_z}{F_x} = \frac{1}{\mu} \tag{38}$$

$$\frac{M}{rF_z} = -\mu \frac{F_x}{F_z} = -1 \tag{39}$$

For Figure 10c, we have

$$M + \ell F_x + \mu r F_z = 0 \tag{40}$$

$$F_z - \mu F_x = 0 \tag{41}$$

or

$$\frac{F_z}{F_x} = \frac{1}{\mu} \tag{42}$$

$$\frac{M}{rF_z} = -(2\lambda + 1) \tag{43}$$

For the other two one-point contacts, one obtains

$$\frac{F_z}{F_x} = -\frac{1}{\mu} \tag{44}$$

$$\frac{M}{rF_z} = 1 \quad \text{or} \quad (2\lambda + 1) \tag{45}$$
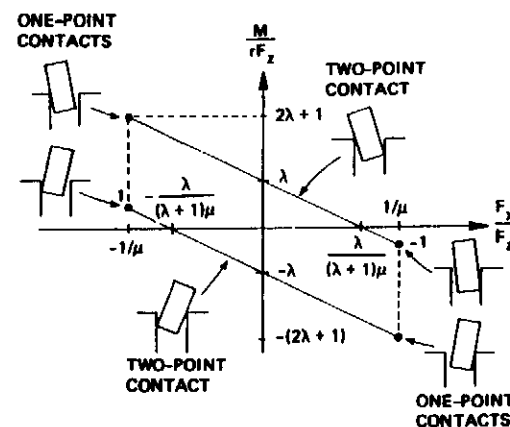
Figure 11
The jamming diagram.

It is easy to show that these four points lie on the two lines which obey equation (30) restated as

$$\frac{M}{rF_z} = \pm\lambda - \frac{F_z}{F_x}\mu(1 + \lambda) \tag{46}$$

In fact, they are the endpoints of these lines because the lines represent just sliding in, i.e.,

$$F_z \geq \mu F_x \tag{47}$$

or

$$\frac{F_z}{F_x} \leq \frac{1}{\mu} \tag{48}$$

for the right-side one-point contacts, and similarly with a minus sign for the left-side ones. Larger F_x/F_z results in one-point contact jams. All of the above can be summarized in Figure 11. The vertical dotted lines in the diagram describe a line contact. Figure 11 may be interpreted as follows. Combinations of F_x, F_z, and M falling on the parallelogram's edges describe equilibrium sliding in. Outside the parallelogram lie combinations which jam the peg, either in one- or two-point contact. Inside, the peg is in disequilibrium sliding or falling in.

Note that as $\lambda \to 0$ (peg shallow in the hole) the parallelogram collapses to a line running between $(1/\mu, -1)$ on the right to $(-1/\mu, 1)$ on the left, showing
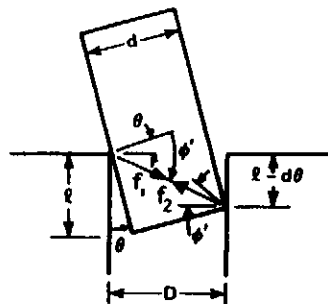
Figure 12
Geometry of wedging condition showing intersection of left and right side friction cones; cone half angle $= \phi' = \tan^{-1} \mu$. Figure drawn for case of largest ℓ for which wedging cannot occur.

that the no-jam region is quite small. When $\lambda \to \infty$, (peg deep in the hole) the parallelogram expands to a vertical strip lying between $-1/\mu$ and $1/\mu$, implying that line and one-point contact jams are still possible, but two-point contact jams are quite difficult to achieve. The F_z/F_x axis intersection of the upper side of the parallelogram is at $F_z/F_x = \lambda/(\lambda + 1)\mu$. A little algebra shows that this must be less than $1/\mu$ for all $\lambda \geq 0$, so Figure 11 shows the general case.

Wedging is also a condition in which the peg appears stuck in the hole, but unlike jamming, the cause is geometric rather than ill-proportioned applied forces. Indeed, wedges can be so severe that no reproportioning of the applied forces can cause assembly to proceed except by damaging the parts at their contact points.

To model wedging we must assume that at least one of the parts is elastic, although it is still stiff compared to K_x and K_θ. In wedging, the two contact forces f_1 and f_2 can point directly toward each other, storing energy in the elastic part. This is possible if two-point contact occurs when ℓ_2 is small, allowing the two friction cones at the contact points to intersect. Figure 12 shows one possible situation, in which ℓ_2 is as large as possible and still allows wedging. The right side contact force does not point along an extreme of the friction cone, indicating that relative motion between the parts on the right side has stopped. The left side contact force points along the lower extreme of the friction cone, indicating that the left side of the peg is attempting to move *out* of the hole. This could occur if the peg has been pushed counterclockwise, elastically deformed at the contact points, and released.

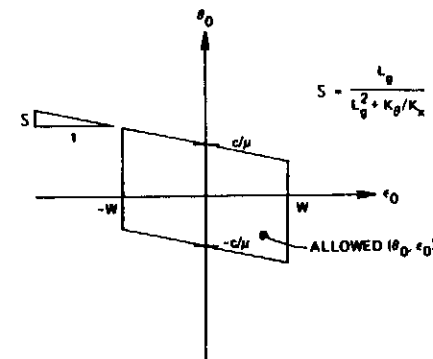Consideration of the geometry in Figure 12 allows us to write

Figure 13
Geometry constraints on lateral and angular error to cross chamfer and avoid wedging.

$$\ell_w = \mu d \tag{49}$$

where ℓ_w is the largest ℓ_2 at which wedging could still occur. The derivation assumes θ and c are both small. Using equation (14) in (49) allows us to define θ_w as the smallest θ_2 at which wedging could occur

$$\theta_w = \frac{c}{\mu} \tag{50}$$

θ_w is noted on Figure 8.

We are now in a position to complete the conditions for successful assembly.
(1) To cross the chamfer we need

$$|\epsilon_0| < w \tag{51}$$

where w is the width of the chamfer (Figure 3).
(2) To avoid wedging, two-point contact must occur at a value of θ_2 obeying

$$|\theta_2| < \frac{c}{\mu} \tag{52}$$

Using equation (19) and assuming ℓ_2 and r are small, we can write

$$\theta_0 + s\epsilon_0 < \pm\frac{c}{\mu} \tag{53}$$

where

$$s = \frac{L_\theta}{L_\theta^2 + K_\theta/K_x} \tag{54}$$

These relations are plotted in Figure 13. Note that when $L_\theta = 0$ there is no interaction between the requirements on ϵ_0 and those on θ_0.
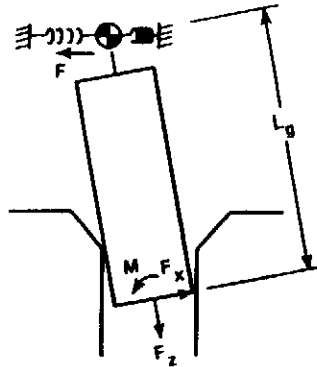
Figure 14
Peg suspended by lateral spring

(3) To avoid jamming, we must maintain

$$\left| \frac{M}{rF_z} + \mu(1 + \lambda)\frac{F_x}{F_z} \right| < \lambda \tag{55}$$

and

$$\left| \frac{F_x}{F_z} \right| < \frac{1}{\mu} \tag{56}$$

5. Insertion Forces, Jamming Avoidance, and the Remote Center Compliance

The Remote Center Compliance (RCC) is a passive device which supports parts and aids their assembly. It can be modeled by Figure 2 to good accuracy, except that, by design, the RCC succeeds in placing the support point or compliance center at or near the tip of the peg. That is, L_g is nearly zero. In this Section, the RCC will be described by a simplified model having $K_\theta = 0$. This makes it easier to show how the RCC avoids jamming, how relatively unimportant it is to make L_g exactly zero, and how the insertion force varies if L_g is not zero.

5.1 Model of the RCC as Lateral Stiffness Alone. Refer to Figure 14, where the simplest compliant suspension is shown, one with only lateral stiffness.

The situation shown in the Figure can occur if the peg is initially in error to the left of the hole, where the springs are relaxed. The peg tilts, as shown, while crossing the chamfer, and rocks clockwise during two-point contact. This stretches and squeezes the springs as indicated.

The force and moment applied by the lateral springs can be re-expressed in peg tip coordinates as

$$F_x = -F \tag{57}$$
$$M = L_g F = -L_g F_x \tag{58}$$

Dividing equation (58) by rF_z, one obtains

$$\frac{M}{rF_z} = -\frac{L_g}{r}\left(\frac{F_x}{F_z}\right) \tag{59}$$

which means that M, F_z, and F_x will lie on a line in Figure 11 having slope $-L_g/r$ and passing through the origin. This line will intersect the parallelogram at

$$\frac{F_x}{F_z} = \pm\frac{\lambda}{L_g/r - \mu(1 + \lambda)} \tag{60}$$

or at

$$\frac{F_x}{F_z} = \pm\frac{1}{\mu} \tag{61}$$

if the intersection is on the vertical sides of the parallelogram. Since the amount of lateral error and K_x determine F_x, we see that insertion can occur only if F_x is big enough to satisfy (60) or (61).

5.2 Relation Between the Value of L_g and the Jamming Diagram. Let us study the effect of different values of L_g. The intersection points move farther horizontally left and right as L_g/r is made smaller. When we have

$$\frac{L_g}{r} = \frac{\ell}{r} + \mu \tag{62}$$

we obtain the condition of equation (61), that is, we just maintain equilibrium in one-point contact, as shown for the upper left corner of the parallelogram by Figure 15. Note that to maintain this equilibrium, the point $\otimes$ where the spring attaches must remain fixed in space with respect to the *hole*. The necessary F_x for given F_z is smallest at this point. Also, F_x/F_z and M/rF_z can be permitted wider variations without threatening an occurrence of jamming. For these reasons, the RCC attempts to locate the support point close to the tip of the peg or mouth of the hole, where equation (62) is satisfied approximately. If L_g gets a bit smaller, the peg will suddenly snap over clockwise into a line contact, and maintain this equilibrium until L_g/r reaches
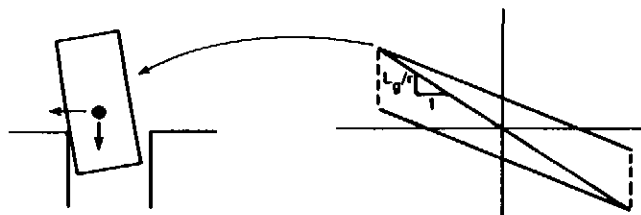
$$\frac{L_g}{r} = \mu \tag{63}$$

Figure 15
Combination of equation (59) and Figure 11 for the case of peg compliantly held by lateral spring at point $L_g = \ell + r\mu$ from tip of peg.
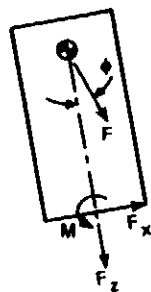

Figure 16
Peg-pulled along F by a string.

at which point the peg will be in a precarious equilibrium in the other left side one-point contact. Further lowering L_g will cause the peg to snap into two-point contact of the opposite sense from that shown in Figure 15. For stable equilibrium in this condition (without changing the sign of c_0) we need $L_g \leq 0$.

Note finally that, with the spring pulling to the left, the right side one-point contacts cannot occur.

A more complex analysis below takes into account suspensions having torsional stiffness as well. We can predict in advance that the line of slope L_g/r will not pass through the origin of Figure 11.

5.3 Model of a Peg Pulled by a String or Pushed by a Slender Rod. This case represents a pure force (no moment) applied to a point on the peg, corresponding in many ways to Figure 14 (see Figure 16). It is easy to show

---
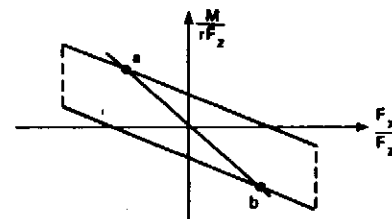
Figure 17
Equilibrium sliding conditions for peg pulled by string. Point a corresponds to the sliding solution when $\phi < 0$, while point b corresponds to $\phi > 0$.

that

$$\frac{M}{rF_z} = -\frac{F_z L_g}{F_z r} = -\frac{L_g}{r}\tan\phi \qquad (64)$$

which is the same as equation (59) and is diagrammed in Figure 17.

Although the two cases (spring and string) have the same equation, there is a difference. When the peg is pulled by the string, F_x and F_z are proportional to each other, while in the case of lateral spring support F_x comes from the spring and F_z is an independent pushing force. Therefore in the spring support case one can make F_x/F_z and M/rF_z smaller by making F_z bigger, so that a jammed peg can be unjammed merely by being pushed harder. But equation (64) shows that M/rF_z depends only on L_g/r and the angle of the string. If the latter are too large, M/rF_z will be too large regardless of $|F_z|$ and the peg, if jammed, will stay jammed.

The reason for pursuing this exercise is that the string/rod model represents a common error-absorbing technique called *float*, in which a part is allowed motion in the x direction by a sliding bearing and, possibly, centering strings. Bearing friction will contribute an x force proportional to F_z, possibly resulting in failure to avoid jamming. Therefore, in the presence of angular error, float can be an unreliable technique.

5.4 Relating the Support Point Location L_g and the Pulling Error Angle ϕ to Jamming. This issue applies to both the lateral spring support and the string pulling situations because, if the peg is sliding,

$$\tan\phi = \frac{F_x}{F_z} \qquad (65)$$

in both cases. To relate ϕ to sliding equilibrium, put (65) into (60) to get

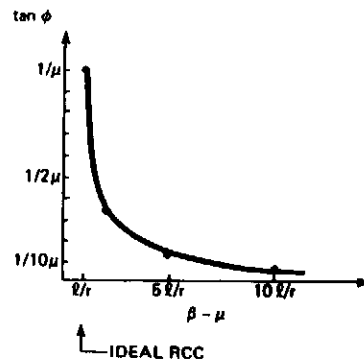$$\tan\phi = \frac{\lambda}{L_g/r - \mu(1+\lambda)} \qquad (66)$$

Figure 18
Worst case ϕ to maintain sliding when wedging can barely occur ($\lambda = 1$).

Abbreviate

$$\frac{L_g}{r} = \beta \tag{67}$$

Let us study two-point contacts in their worst case, namely when $\lambda \approx 1$ where wedging can barely happen. Two-point contact means

$$\beta \geq \frac{\ell}{r} + \mu \tag{68}$$

and this plus $\lambda = 1$ reduces (66) to

$$\tan \phi = \frac{1}{\beta - 2\mu} \tag{69}$$

Using values of β such as

$$\beta = \frac{n\ell}{r} + \mu, \qquad n = 1, 2, 3, \ldots$$

we can graph $\tan \phi$ using equation (69) (see Figure 18).

As a numerical example, let us take $\mu = 0.2$. With $\beta = 10\ell/r + \mu$, $\tan \phi = 5/19$ or $\phi = 14.74$ degrees. Note that, for a clearance ratio of 0.005, the wedging angle is $\tan^{-1}(c/\mu) = 1.43$ degrees. For smaller β, ϕ will be much larger, and is maximum in the RCC where $\beta \simeq \ell/r + \mu$.

Recall that we must point the insertion force vector within $\pm\phi$ of the peg's axis to avoid jamming, and must point the peg's axis within $\pm c/\mu$ of the hole's axis to avoid wedging. In this example, using quite typical numbers, we see that in terms of error angles, jamming is ten times easier to avoid than wedging, even when the center of support of pulling is ten times farther away from the tip of the peg than recommended by equation (62).

The previous discussion shows that the compliance center can be quite far from the tip of the peg and still provide jamming avoidance. It is important to realize that the analysis ignores the fact that the peg is tilted so that an insertion force along the peg is not along the hole axis and vice versa. This means that the allowable ϕ region is not symmetric about the peg's axis. When ℓ/d is small, this asymmetry can be significant unless ϕ is several times the wedging angle.

In addition, the value of β affects the amount of insertion force needed. We examine this next.

5.5 How Much Insertion Force is Needed and How This is Affected by Support Point Location. Suppose the peg is supported laterally by a spring of stiffness K_x as in Figure 14. Repeating equation (46)

$$\frac{M}{r} + \mu(1 + \lambda)F_z = \lambda F_x \tag{46}$$

and describing the compression of the spring by U, we have

$$F_x = -K_x U \tag{70}$$
$$M = -L_g F_x = K_x L_g U \tag{71}$$

Putting (71) into (46), and using

$$\lambda = \frac{\ell}{2r\mu}$$

yields

$$F_z = K_x U \mu \left[2\frac{L_g}{\ell} - \frac{1}{\lambda} - 1 \right] \tag{72}$$

which says that F_z depends linearly on K_x, U, μ, and L_g. The RCC attempts to put

$$L_g = \ell + r\mu$$

to achieve a one-point contact equilibrium. This reduces equation (72) to

$$F_z = K_x U \mu \tag{73}$$

the force created by a one-point contact. For given K_x, μ, and U this is the smallest F_z obtainable, save for no contact force at all.

6. Insertion Force When Peg is Supported by Both Lateral and Angular Compliances

We present here models for the insertion force during chamfer crossing, one-point contact, and two-point contact when the peg is supported by both lateral

and angular springs. To obtain F_z during chamfer crossing, we substitute (7) and (8) into (6) to yield

$$F_z = \frac{K_z K_\theta \Lambda(z/\tan\alpha)}{(K_z L_\theta^2 + K_\theta)B - K_z L_\theta r \Lambda} \quad (74)$$

To obtain F_z during one-point contact, substitute (10) and (11) into the force balance equations for one-point contact to yield

$$F_z = \frac{\mu K_z K_\theta(\epsilon_0' + \ell\theta_0)}{C(L_\theta - \ell) + K_\theta} \quad (75)$$

To obtain F_z during two-point contact, substitute (14) and (17) into (66) to yield

$$F_z = -K_z L_\theta(\theta_0 - \frac{cD}{\ell}) - K_z \epsilon_0'' \quad (76)$$

$$M = (K_z L_\theta^2 + K_\theta)(\theta_0 - \frac{cD}{\ell}) + K_z L_\theta \epsilon_0'' \quad (77)$$

Putting these into (46) yields

$$F_z = \frac{2\mu}{\ell}\left[D(\theta_0 - \frac{cD}{\ell}) + E\right] + \mu(1 + \frac{\mu d}{\ell})\left[F(\theta_0 - \frac{cD}{\ell}) - \frac{E}{L_\theta}\right] \quad (78)$$

where

$$D = K_z L_\theta^2 + K_\theta \quad (79)$$
$$E = K_z L_\theta \epsilon_0'' \quad (80)$$
$$F = -K_z L_\theta \quad (81)$$

Differentiating (78) with respect to ℓ and setting the result equal to zero yields ℓ^*, the value of ℓ where F_z and the contact forces f_1 and f_2 are maximum

$$\ell^* = \frac{(4D + 2F\mu d)cD}{2D\theta_0 + F(1 - \mu d/L_\theta) + F(\theta_0\mu d - cD)} \quad (82)$$

When $L_\theta = \mu r$ this reduces to

$$\ell^* = \frac{4K_\theta cD}{2K_\theta \theta_0 - K_z \mu r \epsilon_0'} \quad (83)$$

The stiffnesses and initial errors influence the result in each instance but it is often true that $K_\theta \theta_0 \gg K_z \mu r \epsilon_0'$. In this case

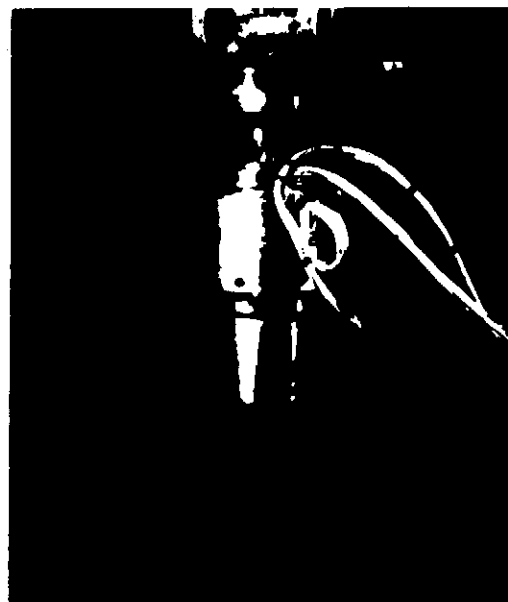$$\ell^* = \frac{2cD}{\theta_0} \simeq 2\ell_2 \quad (84)$$

Figure 19
Photo of the apparatus used to verify equations (74), (75), (78), and geometric relations during part mating. A hardened and ground steel peg is supported by an RCC whose deflections can be measured using integral optical sensors. In this way ϵ and θ of the peg can be recorded during insertion. The RCC is in turn held by a 6 axis force/torque sensor with 10 gram threshold. This allows F_z, F_r and M to be recorded as well. Finally, the sensor is held in the quill of a milling machine whose motion is measured by an LVDT, allowing ℓ to be recorded.

That is, insertion and contact forces are maximum at an insertion depth which is about twice the depth at which two-point contact first occurs. Substitution of (82) into (78) gives the maximum value of F_z. The peak contact force is approximately this F_z divided by 2μ.

Experiments were designed to test equations (74) through (82). The parameters were as follows:

Support (a Draper Lab Model 4B RCC):

$K_z = 7$ N/mm

$K_\theta = 53000$ N-mm/rad

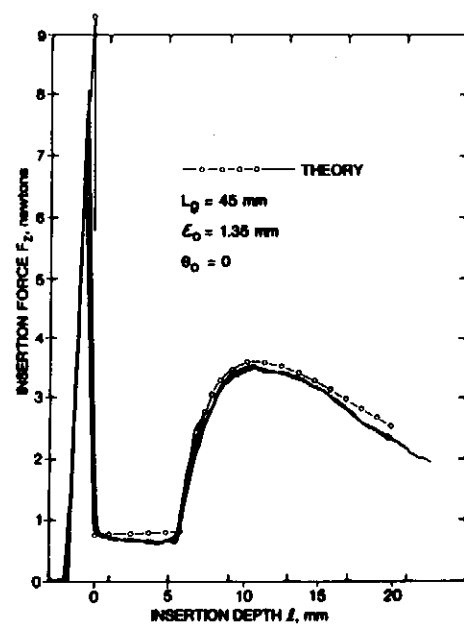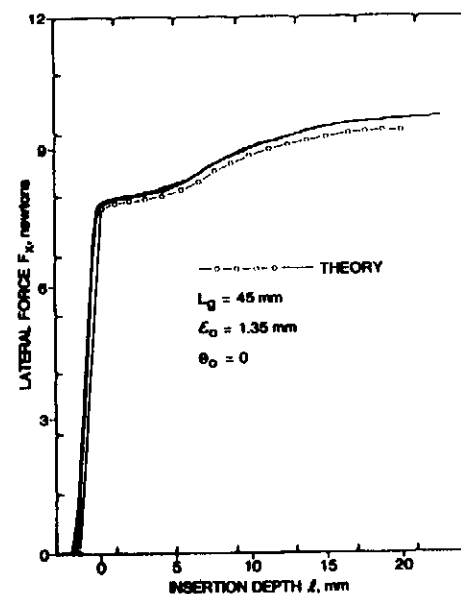*Peg and Hole* (steel, hardened and ground):

Figure 20
Comparison of theory and experiment: insertion force versus insertion depth with support point 45 mm from tip of peg.

Hole diameter $= 0.5002$ inches (12.705 mm)

Peg diameter $= 0.4989$ inches (12.672 mm)

$$c = 0.0026$$

Initial errors:

$\epsilon_0 = 1.4$ mm and 0.85 mm

$\theta_0 = 0$

Location of support:

$L_g = 45$ mm and 1 mm (achieved by using two pegs of different lengths)

Coefficient of friction:

$\mu \approx 0.1$ (determined empirically from one point contact data)

Figure 19 is a photograph of the apparatus.

Figure 21
Comparison of theory and experiment: lateral force versus insertion depth with support point 45 mm from tip of peg.

Figure 20 gives the results of insertion force versus ℓ for $L_g = 45$ mm and $\epsilon_0 = 1.35$ mm, while Figures 21 and 22 show net lateral force F_x and moment M. Figure 23 shows insertion force for $L_g = 45$ mm and $\epsilon_0 = 0.83$. Finally, Figure 24 shows the insertion and lateral force when $L_g = 1$ mm. As predicted, two-point contact does not occur. Figure 25 compares the peg's angle θ versus ℓ with the theory of Section 3. Angle data were obtained using an Instrumented RCC (IRCC). See [De Fazio 1980, Seltzer 1979] for descriptions and other uses of the IRCC.

In all cases, theory and experiment agree as to general trends, and compare fairly well as to absolute magnitudes. Since geometry, K_x, K_θ, and μ cannot be known exactly, one can get better "agreement" between theory and experiment by searching for "better" values of these parameters. Such a search would only improve our knowledge of these values, however, and would not increase our understanding of the problem.
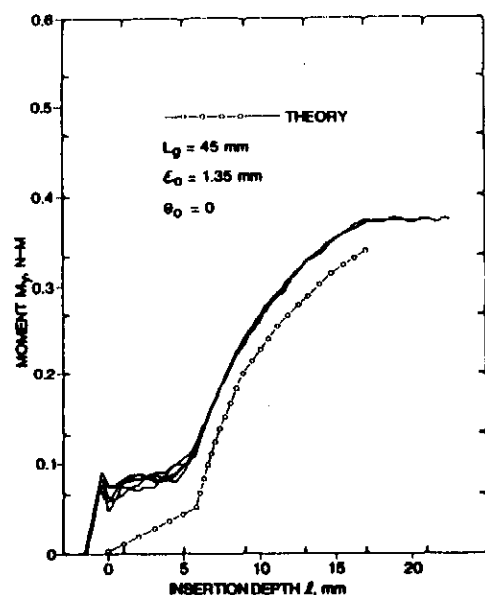
Figure 22
Comparison of theory and experiment: moment normal to insertion axis versus insertion depth with support point 45 mm fro tip of peg.

7. Analysis of Wedging

The other phenomenon which can occur in addition to jamming is called wedging. Analysis of this case must assume some deformation in the parts. The forces acting are shown in Figure 12, where the contact forces point toward one another. If an insertion force is applied, and the parts allowed to deform, then if the jamming conditions are satisfied, the contact forces will move to the upper boundaries of the friction cone and insertion will occur. At some point the peg, perhaps damaged, will be deep enough into the hole that wedging can no longer occur. The contact forces now can exert a couple about the tip of the peg and turn it parallel to the hole. Prior to this point there was little or no moment, misalignment was not corrected, and high insertion and contact forces occurred. We analyze these forces below, using numerous assumptions. A similar analysis appears in [Drake 1977].

The situation shown in Figure 26a is that of a wedged peg which, when pushed by F_z does not turn clockwise but instead compresses. This is approximately
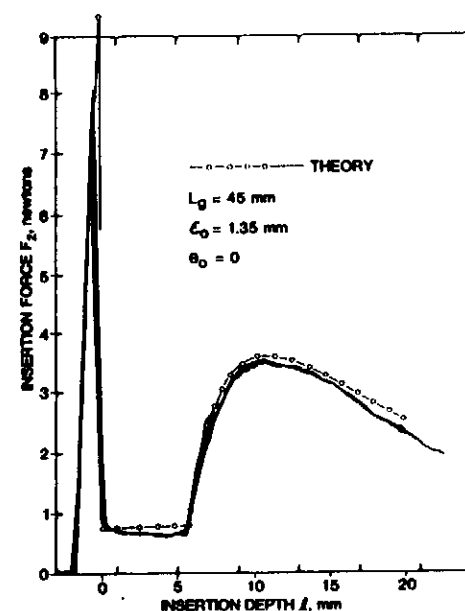
Figure 23
Comparison of theory and experiment: insertion force as in Figure 20 except lateral error is smaller.

equivalent to the case shown in Figure 26b. We intend to use Hertz stress analysis (not totally appropriate) to analyze this case. To do so, we split and image the peg axially, so that the contact point can be represented as an edge of small radius of curvature. Figure 26b can be analyzed to yield

$$F_z = 2f_1(\mu + \frac{\theta}{2}) \tag{85}$$

and Figure 26c can be analyzed to yield

$$Q = f_1 \tag{86}$$

On the assumption that, for most machined part, $\theta < \mu$, we have
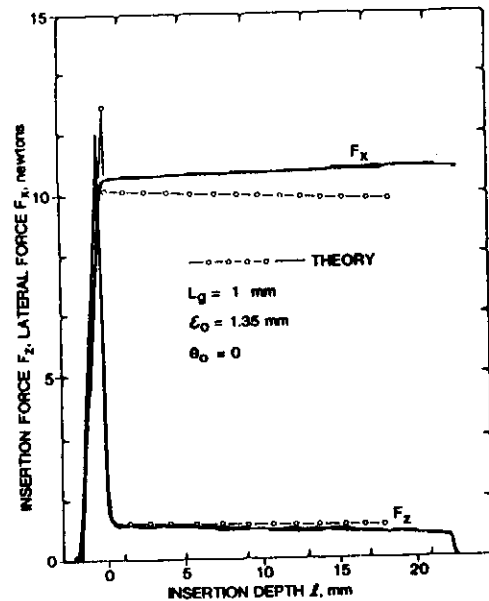
$$Q \simeq \frac{F_z}{2\mu} \tag{87}$$

Figure 24
Comparison of theory and experiment: insertion force and lateral error as in Figure 20 except support point is almost exactly at tip of peg.

A Hertz stress analysis will be used to find the deflection δ at each contact point. The geometric relation between δ and incremental insertion motion Δ

$$\Delta = \frac{\delta}{\theta} \tag{88}$$

will be used to see how far the peg can move into the hole for given δ. The result is probably an underestimate since the Hertz analysis ignores shear stress, which is large in our case.

The Hertz analysis models the hole as a concave body with curvatures

$$\rho_1 = -\frac{1}{R} \tag{89}$$

and

$$\rho_2 = 0 \tag{90}$$
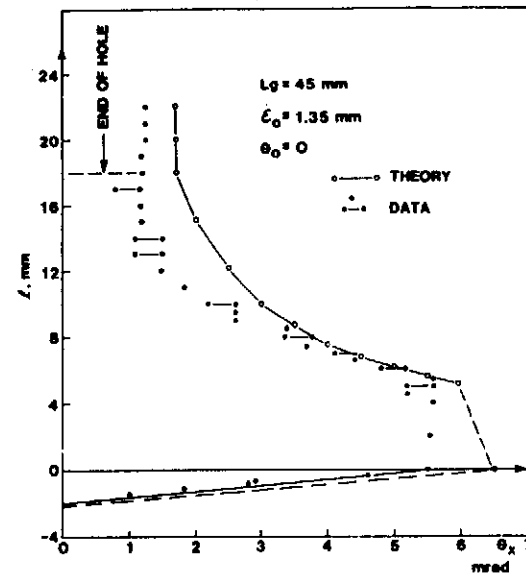
Figure 25
Comparison of theory and experiment: conditions as in Figure 20. Plot of inclination angle θ versus insertion depth ℓ.

while the peg is modeled as an ellipsoid with

$$\rho_1 = \frac{1}{R} \tag{91}$$

and

$$\rho_2 = \frac{1}{\beta r} \tag{92}$$

with $\beta \ll 1$ to indicate a sharp corner.

Following the procedure in Harris [1966] and using

$\mu = 0.2$

$r = 6.35$ mm

$R = 6.35635$ mm (corresponding to $c = 10^{-3}$)

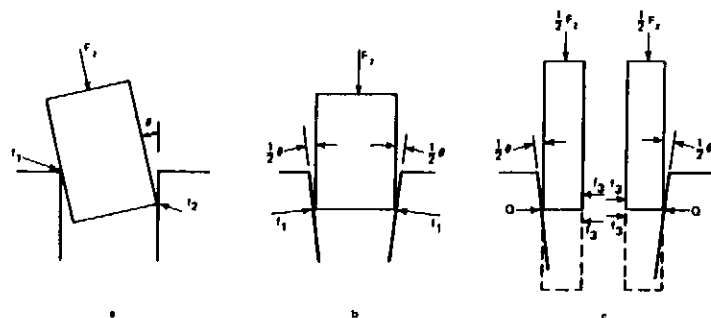$\beta = 10^{-2}$

$\theta = 5 \times 10^{-3} = c/\mu$

Figure 26
Forces acting in wedging.

we obtain the results shown in Table 1, assuming steel peg and hole. Even with 222 Newtons insertion force the peg moves more than $r/10$ into the hole, indicating that many wedges apparently can be relieved if sufficient force is used and galling or other damage can be tolerated. However, quite high stresses may occur.

These results may explain the apparent fact that wedging does not seem to occur in machine-aided assembly, although it often occurs in manual assembly. Probably, wedging does occasionally occur but the assembly apparatus is strong enough to force the parts past the wedging region.

8. Conclusions

Geometric and force-deformation analyses for rigid part mating have been presented, covering the main geometric phases of assembly plus the phenomena of wedging and jamming. The ability of the RCC to reduce mating forces and the chance of jamming has been explained. The models have been verified by experiments. These results allow calculation of allowed lateral and angular error limits plus tolerance on the ideal location of the compliance center. If maximum

$F_z N$	$Q N$	δ mm	Δ mm
44.5	111.25	1.6×10^{-3}	0.32
222	556.25	4.57×10^{-3}	0.934
445	1112.5	7.36×10^{-3}	1.47
2222	5562.5	2.16×10^{-2}	4.34
4450	11125	3.56×10^{-2}	6.91

Table 1. Results of wedging analysis.

allowed values of the contact forces are known, then this plus maximum allowed errors permit calculation of good values for K_z and K_θ.